Periodic Grain Boundary Grooves: Analytic Model, Formation Energies, and Phase-Field Comparison

Martin E. Glicksman[1,2] · Peichen Wu[3] · Kumar Ankit[3]

Abstract Analytic profiles for periodic grain boundary grooves (PGBGs) were determined from variational theory. Variational profiles represent stationary solid-liquid profiles with abrupt, zero-thickness, transitions between adjoining phases. Variational PGBGs consequently lack tangential interfacial fluxes, the existence of which requires more realistic (non-zero) interfacial thicknesses that allow energy and solute transport. Variational profiles, however, permit field-theoretic calculations of their scaled formation free energy and thermodynamic stability, capillary-mediated chemical potentials, and their associated vector gradient distributions, all of which depend on a profile's geometry, not its thickness. Despite the fact that variational profiles are denied interface fluxes, one may, nevertheless, impute shape-dependent interface transport in the form of a profile's surface Laplacian of its presumptive chemical potential distribution due to capillarity. We compare variational surface Laplacians with residuals of the thermo-chemical potential measured along counterpart diffuse-interface PGBGs, simulated via phase-field with metrically-proportional profiles. Fundamentally, it is the thickness of a microstructure's interfaces and its shape that co-determine whether, and to what extent, gradients of the chemical potential excite fluxes that transport energy and/or solute. PGBGs, both variational and simulated, greatly expand the limited universe of solid-liquid microstructures suitable for *steady-state* thermodynamic analysis. Understanding the origin and action of these capillary-mediated interfacial fields opens a pathway for estimating and, eventually, measuring how solid-liquid interface thickness modifies the transport of energy and solute during solidification and crystal growth, and influences microstructure.

✉ Martin E. Glicksman
mglic@mse.ufl.edu; mglicksman@fit.edu

Peichen Wu
peichenw@asu.edu

Kumar Ankit
kumar.ankit@asu.edu

1 Department of Materials Science and Engineering, University of Florida, 100 Rhines Hall, Gainesville, FL 32611-6400

2 Professor Emeritus, Florida Institute of Technology, Melbourne, Fl 32901

3 Materials Science and Engineering, School for Engineering of Matter, Transport, and Energy, Arizona State University, 551 E. Tyler Mall, Tempe, AZ 85287-6106

Keywords capillarity · grain boundary grooves · interface stability · phase-field modeling · solid-liquid interfaces · surface Laplacian · surface thermodynamics

1 Introduction and System Description

1.1 Background and Approach

Dynamic analysis of periodic grain boundary grooves was first mentioned by P.A. Martin,[1] as part of his extension of W.W. Mullins's original study of solid-vapor grain boundary grooving kinetics.[2, 3] Our interest here, however, is in probing the steady-state behavior of solid-liquid (s/ℓ) grain boundary grooves, to gain further insight into

the nature of s/ℓ interfaces. Periodic grain boundary grooves (PGBGs) are well suited for that purpose. They provide microstructures more adaptable to thermodynamic analysis than do previously used isolated grain boundary grooves (GBGs). Isolated GBGs are available as the first s/ℓ variational profiles subjected to detailed mathematical analysis, accomplished some 60 years ago by Bolling and Tiller,[4] This paper, in part, extends their variational analysis to PGBGs.

In a chapter titled *"Plateau's Problem"*, published in "The World of Mathematics",[5] mathematicians Richard Courant and Herbert Robbins state, *"It is very difficult, and sometimes impossible, to solve variational problems explicitly in terms of formulas or geometrical constructions involving known simple elements."* See also.[6] These distinguished mathematicians then proceed to use soap-film experiments as physical demonstrations that support well-established results derived from the variational calculus, even disclosing the behavior of several mathematically unproven variational problems. Their fascinating chapter shows that some "very difficult"—even unsolved—solutions in variational calculus can be visualized through experiment.

The present study parallels, perhaps in a reverse sense, the Courant/Robbins approach: we first solve the variational problem of periodic grain boundary grooves, to ascertain from their profiles a sub-set of their steady-state capillary-mediated thermodynamic fields. Then by simulating proportionately shaped profiles, using numerical "experiments" in the form of a phase-field model, obtain both direct visualization of these s/ℓ microstructures and measurements of their interfacial chemical potentials. Comparative data derived from variational theory and measured independently from simulations, provide quantitative support for the existence of a variety of capillary-mediated phenomena. The combined exercise, viz., variational calculus coupled with phase-field numerical analysis, yield significant new insights into the thermodynamic behavior of real s/ℓ interfaces.

We first derive the analytic solution to a non-linear ordinary differential equation (ODE) that describes steady-state variational profiles for PGBGs. These profiles have interfaces of zero thickness, which are treated as mathematical manifolds with surface tension. In that unrealistic limit of perfectly thin s/ℓ interfaces, transport of energy or matter is, of course, precluded within the plane of their profiles. Nevertheless, application of classical field theory to variational profiles still easily discerns the precise origin and details of a PGBG's first- and even higher-order thermodynamic fields.

Moreover, for every such scalar or vector capillary-mediated field identified as being resident, or potentially resident, on variational profiles, there should exist an equivalent field on similarly-shaped profiles of real, or simulated, s/ℓ interfaces. The major distinction between the fields acting on a variational interface, and those on real or simulated diffuse interfaces, is that the latter two cases possess finite interfacial thicknesses that can transport tangential flows of energy and solute. Capillary-mediated tangential flow along curved s/ℓ interfaces, however, remains to date a little explored topic, with possible practical applications that could lead to improved deterministic microstructure control in metal casting, welding, and crystal growth.

In this study, the concatenation of scalar and vector capillary fields mentioned above, ends with finding their surface Laplacians of the interfacial chemical potential. The surface Laplacian is a standard 4th-order scalar field, derived from the profile of a variational interface. This Laplacian equals, or closely approximates, the flux divergence present on a simulated diffuse-interface microstructure, having a shape (curvature distribution) that is proportional to its counterpart variational profile. Diffuse-interface microstructures are simulated with a multiphase-field model. Phase-field models develop reasonably realistic microstructures from many sequential computational steps that solve and re-solve coupled partial differential equations (PDEs) representing the laws of chemical thermodynamics. Importantly, these PDEs are governed by the same geometric and thermal constraints—the boundary conditions—that are used to calculate their counterpart variational profiles.

In sum, variational PGBG shapes, with exactly known curvature distributions, establish through field theory the thermodynamic origin and interpretation of their interfacial fields. Interface potential measurements are obtained independently from numerical simulations of nearly identically-shaped diffuse-interface microstructures. These carefully linked procedures provide independent outputs from variational theory and numerical simulation. Their comparison allows definitive verification of the thermodynamic origin of interfacial energy sources and sinks, and quantitative checks on their distributions of chemical potential. In addition, using PGBGs to implement this coordinated approach adds a useful extra degree of freedom to the limited class of steady-state microstructures found suitable, thus far, as test cases for their interfacial fields. We briefly explore how different interfacial thicknesses influence capillary-mediated energy fields that affect interface transport in a phase-field model, and hope that eventually that deterministic methods are developed to influence pattern formation during solidification and crystal growth.[7–9]

1.2 System Specification

The case of variational PGBGs is considered first. These microstructures develop from parallel grain boundaries intersecting, retracting, and curving an initially planar s/ℓ interface. Mirror symmetry at each grain boundary intersection, or triple junction, produces a periodic microstructure, Fig. 1. Analytic steady-state profiles for PGBGs with *sharp* interfaces, as already mentioned, yield to standard field-theoretic methods to predict their interfacial temperature and distribution of chemical potential. For one-component systems at constant pressure, which comprise the microstructures considered in this study, the temperature variation along a curved s/ℓ interface may be accurately predicted using the standard Gibbs-Thomson relation,[10] which provides the chemical potential distribution established by local two-phase equilibria. Field theory then predicts the associated interfacial gradient structure of the chemical potential, and the occurrence of any scalar divergences within those vector fields. Divergences of gradients and their imputed interfacial fluxes are calculated here as the surface Laplacian of the thermochemical potential. The surface Laplacian, as one finds later, manifests itself as a steady-state distribution of energy sinks and sources along diffuse-interface PGBGs.

Variational models for PGBG profiles are described by an ordinary differential equation (ODE) that was formulated, solved, and checked with an appropriate Euler-Lagrange equation.[11] A basic formulation of these objects will be presented here to inform the reader of what factors control their form and function. The solid and liquid phases
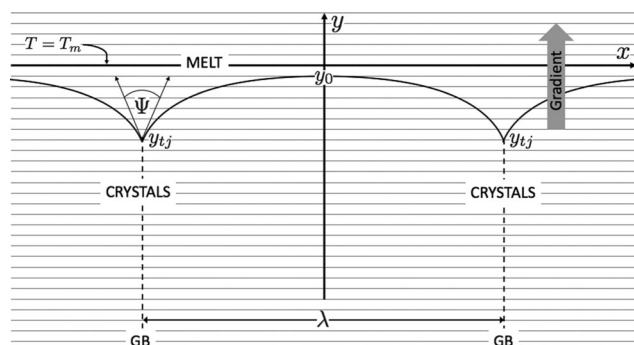

Fig. 1 Physical configuration of a periodic grain boundary groove (PGBG) profile. Periodic triple-junction coordinates are located at $x = \pm n\lambda/2, y = y_{tj}, \; n = 1, 3, 5 \ldots$. The profile's midpoints are at $x = \pm m\lambda, \; y = y_0, \; m = 0, 1, 2, \ldots$. The midpoint ordinates, $y_0 < 0$, are the uppermost and warmest interface points, always located below the system's melting point isotherm, T_m, which is at $y = 0$. The dihedral angle, Ψ, paired with the GB spacing, λ, are parameters that conventionally determine a PGBGs profile. A grid of horizontal lines represents the distribution of isotherms, $T(y; G)$, that support a uniform temperature gradient, G, with steady heat flux over the entire x-y plane. Time-independent uniform heat flow requires equal thermal conductivities and molar volumes for both phases

considered here are assumed to have identical thermal conductivity and molar volume. These assumptions allow the constraining thermal field applied to the two-phase system to remain spatially linear and independent of the s/ℓ interface.[12]

As indicated in Fig. 1, a PGBG's repeat distance, λ, is the space between adjacent triple junctions. The dihedral angle, Ψ, satisfies local force equilibrium at triple junctions, via Young's vector law, considered here as a "natural boundary condition" in the variational problem, which allows mechanical equilibrium among the interfaces forming each triple junction.[13]

Values of a profile's ordinates, $y(x)$, remain negative everywhere along the s/ℓ interface. The x-axis is coincident with the system's melting point isotherm, T_m, and remains positioned above a profile's midpoint, so $y_0 < 0$. Moreover, midpoints locate the warmest and least curved locations along a PGBG's profile. The 1-D temperature field, $T(y; G)$, provides a uniform gradient constraint, $\mathbf{G} = (dT/dy) \cdot \mathbf{j}$, that points in the $+y$ direction, and is the organizing field constraint that controls the entire microstructure. A PGBG's profile is therefore collectively determined by the magnitude of this applied gradient, G, the grain boundary energy density, γ_{gb}, the spacing between adjacent boundaries (GB), λ, and lastly, the crystal-melt interfacial energy density, $\gamma_{s\ell}$, the latter assumed to be isotropic. These material and system properties determine the dihedral angle, Ψ, and locate the ordinate position of a profile's steady-state triple-junctions, y_{tj}, relative to the melting point isotherm at $y = 0$.

The case of mild crystal-melt anisotropy, attributable to many real systems, where $\gamma_{s\ell}$ varies less than a few percent with crystallographic orientation to the melt, one finds that variational shapes still closely approximate experimentally observed groove profiles.[14, 15, 27] Faceted interfaces, which are often encountered in the case of solid-vapor GBGs, display singular jumps in their curvature distributions, and require a different category of variational profiles that incorporate discontinuities in their angular interfacial free energy densities.

An isometrically scaled dimension-free PGBG profile is illustrated in Fig. 2. This profile extends a scaled distance $\Delta_\mu \equiv \lambda/2\Lambda$, which repeats periodically in the $\pm\mu$-directions. The characteristic thermo-capillary scaling length, Λ [m], defined in Eq 1, is introduced to define dimensionless Cartesian coordinates: viz., $\mu = x/2\Lambda$ and $\eta = y/2\Lambda$, as well make dimension-free all other length-dependent quantities, including interfacial arc-length and curvature, and potential gradients. Cf. Fig. 1 and 2.

Intersections between grain boundaries and the solid-liquid interface occur as triple-junctions. These features locate periodically at $\mu_{tj} = \pm n\Delta_\mu/2 \; (n = 1, 3, 5, \ldots)$. Triple
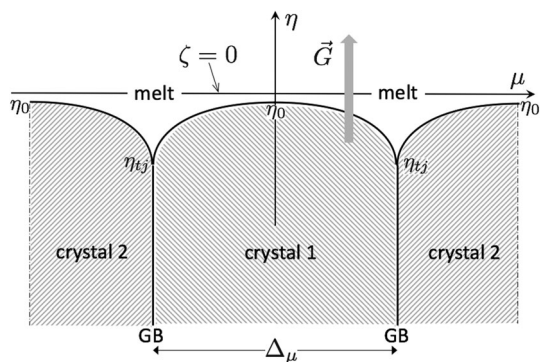
J. Phase Equilib. Diffus. (2022) 43:718–737

721

Fig. 2 Periodic dimensionless PGBG profile in quadrants III and IV of the (μ, η)-coordinate system, which are scaled Cartesian coordinates that replace the physical (x, y) coordinates used in Fig. 1. The value of Λ, the thermocapillary scaling length, depends primarily on the magnitude of the arbitrary temperature gradient, **G**, in the $+\eta$ direction. The scaled profile, $\mu(\eta) = \mathcal{U}(\eta; \eta_0, \Psi)$, occupies a limited region in (μ, η)-space, over which the η-coordinate oscillates between the triple junctions, η_{tj}, where the dimensionless curvature, $\hat{\kappa}(\eta_{tj})$, is largest, to its midpoint, η_0, where the curvature, $\hat{\kappa}(\eta_0) > 0$, is smallest, and so on. The interface's profile repeats along the $\pm\mu$-axes, as determined by its scaled triple junction spacing, $\Delta_\mu \equiv \lambda/2\Lambda$

junctions uniformly retract to their steady-state ordinates η_{tj}. They "drag" the s/ℓ interface downward, and configure its profile to reduce the system's free energy. Midpoints occur at ordinates $\eta_0 < 0$. Dimension-free temperatures are designated in this setting as the scaled linear potential distribution, $\zeta(\eta) \equiv (T(y) - T_m)/2\Lambda G$.

The scaled PGBG system represents a constrained, dimension-free, steady-state microstructure. Each phase supports the applied thermal gradient and allows steady heat-flow. Although such a microstructure is unchanging, it is clearly *not* at thermodynamic equilibrium, as its bulk phases support a uniform gradient with its attendant heat flow and entropy production. In fact, it is *only* the s/ℓ interface itself that achieves *local* equilibrium. More precisely, at a fixed melt pressure, P, a chemical potential distribution, $\zeta_{int}(\eta(\mu); \mathbf{G}, P)$, develops at steady-state along the curved interface. The interface is embedded in the macroscopic temperature gradient, **G**; its profile, now and forever, satisfies the thermochemical potential and curvature distributions required by local thermodynamic equilibrium. Entropy, nevertheless, continues to be produced steadily by this constrained microstructure.

The s/ℓ interface, at local equilibrium, however, satisfies thermal, mechanical, and chemical equilibria, all of which are governed by both the dihedral angle and the Gibbs-Thomson effect. The Gibbs-Thomson relation is the linearized version of Kelvin's equation,[10, 16] that applies to pure *condensed* phase-pairs—crystal and its melt—separated by a curved interface of zero thickness and isotropic energy density. At steady-state, the temperature gradient and pressure imposed on the interface combine to

establish compatible distributions of the Gibbs-Thomson temperature, or thermochemical potential, $\zeta_{int}(\eta(\mu))$, and local curvature, $\hat{\kappa}(\eta(\mu))$. Both of these quantities for the scaled system are defined more exactly in the next section, where thermodynamics engages geometry.

1.3 Microstructure Scaling

Variational PGBG profiles are planar curves described by an as yet unknown 2-D profile, $\mu(\eta) = \mathcal{U}(\eta; \lambda, \Psi)$, that repeats over the dimensionless interval $\Delta_\mu = \lambda/2\Lambda$. The characteristic thermo-capillary length, Λ [m], chosen to scale physical distances, curvatures, and temperature gradients, derives from the Euler-Lagrange variational equation,[11] used to solve the original (non-periodic) GBG profile.[4] Formally, the limit of isolated GBGs is reached as the grain boundary separation widens indefinitely, i.e, as $\Delta_\mu \to \infty$. Any finite Δ_μ value corresponds to a periodic case, as considered next.

The thermo-capillary length, Λ, selected to scale all physical lengths, curvatures, gradients, and energies, is defined as,[9]

$$\Lambda \equiv \sqrt{\frac{\gamma_{s\ell}\Omega}{G\Delta S_f}}. \tag{Eq 1}$$

To evaluate Λ [m] with Eq 1 requires values for the s/ℓ interfacial energy density, $\gamma_{s\ell}$ [J/m²], assumed to be isotropic; the molar volumes of both phases, Ω [m³/mole], assumed to be equal; the magnitude of the applied thermal gradient, G [K/m]; and the system's molar entropy of fusion, ΔS_f [J/mole-K].

The background grid of lines displayed in Fig. 1 represents isotherms of the applied temperature field, the dimensional form of its spatial distribution is the linear field,

$$T(y; G) = T_m + Gy. \tag{Eq 2}$$

1.4 Interface Thermochemical Potential

As mentioned, at steady state the applied thermal field impresses its thermochemical potential distribution on the PGBG profile in the y-direction. An interface potential may be defined in non-dimensional form by substituting interface temperature, $T_{int}(x, y)$, on the left-hand side of Eq 2, and dividing through by a "characteristic" thermocapillary temperature interval, chosen here as $2\Lambda G$ [K]. These steps define a dimension-free thermochemical potential, $\zeta_{int}(\eta(\mu))$, which, at steady-state, also establishes two-phase local equilibria along the interface.

Equation 3 show that the arbitrary magnitude of the temperature gradient, **G**, in Eq 2, the interface's vertical

722

J. Phase Equilib. Diffus. (2022) 43:718–737

coordinate, $y(x)$, and the system's scaling length, Λ, all combine as a dimensionless interface thermopotential, $\zeta_{int}(\eta(\mu))$, which conveniently equals the interface's η-coordinate:

$$\zeta_{int}(\eta(\mu)) \equiv \frac{T_{int}(y(x); \lambda, \Psi) - T_m}{2\Lambda G} = \frac{G\,y(x)}{2\Lambda G} \equiv \eta(\mu).$$
(Eq 3)

1.5 Interfacial Curvature

The relationship between the curvature of a s/ℓ interface and its local thermochemical potential was found through linearization of the classical exponential Kelvin equation for liquid/vapor equilibria at curved interfaces of small droplets. Linearization of Kelvin's law for one-component condensed-phase interfacial equilibria is credited to J.W. Gibbs, and called the Gibbs-Thomson effect.[10, 16]

Classical thermodynamic analysis assumes that s/ℓ interfaces are sharp, Gibbsian "dividing surfaces", with *zero* transition thickness between adjoining phases. The assumption of an abrupt transition between contacting condensed phases is considered necessary for application of the Gibbs-Thomson relation, which requires: (1) perfectly sharp s/ℓ interfaces of uniform energy density, (2) local s/ℓ thermodynamic equilibria, and (3) uniform melt pressure or balanced normal stress. The Gibbs-Thomson effect, moreover, predicts that the local equilibrium interface temperature, T_{int}, and the thermochemical potential, ζ_{int}, decrease with positive (convex) curvature, $\kappa(y(x)) > 0$, and increase with negative (concave) curvature. Convex curvatures occur at s/ℓ interfacial points where a 2-D interface's osculating circle has its center located in the solid phase, whereas concave curvatures occur at points where an interface's osculating circle has its center located in the liquid phase.

Because the shifts in local temperature along typical s/ℓ microstructures caused by curvature and the Gibbs-Thomson effect seldom exceed $\pm 10^{-3}$ K to $\pm 10^{-2}$ K, capillary effects are often disregarded as inconsequential and simply overlooked relative to ambient thermal gradients and bulk fluxes. If one, however, also considers that the associated interfacial distances over which such "tiny" capillary-mediated temperatures and curvature fluctuate, or even change sign—typically 1 [mm] to 10 [nm] in many s/ℓ microstructures—one finds that substantial curvature-induced thermochemical *gradients* are present, and changing at every instant during solidification. Their magnitudes are in the range 1-10^7 [K/m]. Such mesoscopic thermochemical gradients are *not* negligible. Moreover, the time-scale for their local re-equilibration as curvatures evolve is extremely fast, as it equals the thickness of the

s/ℓ interface, squared, divided by the local thermal or solute diffusivity.

A dimension-free form of the Gibbs-Thomson equation can be constructed from the interface potential defined in Eq 3, by equating its linearized relationship to the local interfacial curvature, $\kappa(x, y)$, multiplied by a lumped system constant with the dimension of length, specifically:

$$\zeta_{int}(\eta(\mu)) = \frac{T_{int}(y(x); \lambda, \Psi) - T_m}{2\Lambda G} = -\left[\frac{1}{2\Lambda G}\left(\frac{\gamma_{s\ell}\,\Omega}{\Delta S_f}\right)\right]\kappa(x, y).$$
(Eq 4)

Equation 4 can also be formulated in terms of the interface's dimensionless curvature, $\hat{\kappa}(\eta(\mu)) \equiv \kappa(y(x)) \times 2\Lambda$, as,

$$\zeta_{int}(\eta(\mu)) = -\left[\frac{1}{4\Lambda^2}\left(\frac{\gamma_{s\ell}\,\Omega}{G\Delta S_f}\right)\right]\hat{\kappa}(\eta(\mu)).$$
(Eq 5)

The thermocapillary "area", Λ^2, appearing in the denominator of Eq 5, is defined implicitly by Eq 1, so $\Lambda^2 \equiv \gamma_{s\ell}\Omega/G\Delta S_f$. Substituting this "area" term into the right-hand side of Eq 5 and cancelling unit ratios yields three useful relationships among the interface's thermochemical potential, $\zeta_{int}(\eta(\mu))$, dimensionless curvature, $\hat{\kappa}(\eta(\mu))$, and vertical coordinate, $\eta(\mu)$:

$$\zeta_{int}(\eta(\mu)) = \eta(\mu) = -\frac{1}{4}\hat{\kappa}(\eta(\mu)), \quad [\eta_{tj} \leq \eta(\mu) \leq \eta_0 < 0].$$
(Eq 6)

Equation 6 capture the thermo-capillary physics controlling steady-state profiles of variational PGBGs. Modulo its coefficient of $-\frac{1}{4}$, the interfacial chemical potential, $\zeta_{int}(\eta(\mu))$, equals the local curvature, $\hat{\kappa}(\eta(\mu))$, which underscores the deep connection between interfacial geometry and the system's imposed thermodynamic steady-state.

2 Profile Formulation

2.1 Boundary Conditions

Reflection symmetry across each midpoint, and smoothness of a variational PGBG's slope change over the profile, impose the first boundary condition, namely,

$$\left(\frac{d\eta}{d\mu}\right)_{(\mu=0,\ \eta=\eta_0)} = 0.$$
(Eq 7)

Condition (7), along with the implied presence of interfacial capillarity (surface tension), stipulate zero slope at the midpoints of each periodic unit profile. The melting point, T_m, referred to in the Gibbs-Thomson effect, Eq 4, is the temperature at which equilibrium interface curvatures change sign. T_m, therefore, corresponds to the

thermochemical potential, $\zeta_{int} = 0$, at which a flat s/ℓ interface achieves equilibrium at the system's melt pressure. Consequently, a PGBG profile in quadrants III and IV, where, in accord with condition (7), $\zeta_{int} < 0$, requires *both* a zero slope at each midpoint, η_0, with a positive local curvature, $\hat{\kappa}(\eta_0) > 0$. These coupled geometric requirements at the profile's midpoints satisfy symmetry, the Gibbs-Thomson effect, and the presence of a positive thermal gradient.

The dihedral angle, Ψ, which is the angular slope discontinuity at each triple junction, establishes the allowed eigenrange of continuous slopes over the profile. Specifically, triple junctions start and end each unit profile. When a triple junction is crossed in the $+\mu$ direction, a "jump" in slope angle ensues that is equal to Ψ. Triple junctions denote profile locations that attain maximum curvature, and minimum thermochemical potential. Between triple junctions, continuous non-monotone changes in slope angle occur, from $+\Psi/2$ to $-\Psi/2$, which compensate each jump discontinuity. The terminal slope angles are the complement of the semi-dihedral angle, expressed as boundary constraints at the triple junctions,

$$\left(\frac{d\eta}{d\mu}\right)_{(\mp\mu_{tj},\eta_{tj})} = \pm \tan\left(\frac{\pi-\Psi}{2}\right), \quad [\Psi \in (0,\pi)]. \qquad \text{(Eq 8)}$$

2.2 Differential Equation

The distribution of dimensionless interfacial curvature in 2-D, $\hat{\kappa}(\eta(\mu))$, is described by a standard Cartesian differential form.[17] Equation 9 expresses the relationship among a PGBG's 1st and 2nd derivatives and the profile's steady-state plane curvature distribution, $\hat{\kappa}(\eta(\mu))$[1],

$$\hat{\kappa}(\eta(\mu)) = \frac{-\frac{d^2\eta}{d\mu^2}}{\left[1 + \left(\frac{d\eta}{d\mu}\right)^2\right]^{\frac{3}{2}}}, \quad [\eta(\mu) < 0]. \qquad \text{(Eq 9)}$$

The right-hand equality in Eq 6 already connected curvature at steady-state and an interface's coordinates, viz., $\eta(\mu)$. Equation 6 shows that $-4\eta(\mu) = \hat{\kappa}(\eta(\mu)) > 0$, and links this linear curvature distribution of the s/ℓ interface with the constraining macro-gradient. The governing ODE for the variational profile at steady-state takes the non-linear form,

$$\frac{d^2\eta}{d\mu^2} - 4\eta\left[1 + \left(\frac{d\eta}{d\mu}\right)^2\right]^{\frac{3}{2}} = 0, \quad [\eta(\mu) < 0]. \qquad \text{(Eq 10)}$$

The order of Eq 10 may be reduced by writing its derivatives in terms of the profile's slopes, $p = \frac{d\eta}{d\mu}$, and their first derivative, $dp/d\mu = \frac{d^2\eta}{d\mu^2}$. The reduced-order ODE, subject to conditions already stipulated in Eqs 7 and 8, describes the geometric behavior for the profile slopes,

$$\frac{dp}{d\mu} - 4\eta\left(1 + p^2\right)^{\frac{3}{2}} = 0. \qquad \text{(Eq 11)}$$

The variables $p(\mu)$ and $\eta(\mu)$, that appear in Eq 11, separate by multiplying each term by the inverse slope, $\frac{d\mu}{d\eta} = \frac{1}{p}$, to form the profile's defining ODE:

$$\frac{dp}{d\mu} \cdot \frac{d\mu}{d\eta} - 4\eta\left[\frac{1}{p}\left(1 + p^2\right)^{\frac{3}{2}}\right] = 0. \qquad \text{(Eq 12)}$$

Rearranging Eq 12 and separating variables allow a first integration. Integration extends from the profile's midpoint, η_0, where the first boundary condition specifies a null slope, $p(\eta_0) = 0$, to any general profile point, $\eta(\mu)$, where the slope is $p(\eta)$. The dihedral angle defines the geometry at each triple junction, specifically the discontinuity in slope angle crossing each triple junction. This discontinuity equals the eigenrange of continuous slope angles accumulated across the entire profile. This "range condition" and the corresponding η limits relate two definite integrals,

$$\int_0^p \frac{p}{(1+p^2)^{\frac{3}{2}}} dp = -4 \int_{\eta_0}^{\eta} \eta \, d\eta, \quad |p| \le \tan\left(\frac{\pi-\Psi}{2}\right), \quad \Psi \in (0,\pi). \qquad \text{(Eq 13)}$$

Solving Eq 13 for the slopes of a PGBG's profile yields, after some re-arrangement, the reduced-order ODE for the Cartesian profile, $\mu(\eta)$.

$$p \equiv \frac{d\eta}{d\mu} = \mp\sqrt{\left(\frac{1}{1-2(\eta^2-\eta_0^2)}\right)^2 - 1}, \quad (\eta_{tj} \le \eta \le \eta_0 < 0). \qquad \text{(Eq 14)}$$

The sign of the slopes change across each midpoint, which is a symmetry feature accommodated by accepting both roots on the right-hand side of Eq 14. These roots yield non-linear first-order ODEs for the left and right semi-profiles, $\mu(\eta) = \mp\mathcal{U}(\eta; \eta_0, \Psi)$. As currently expressed in Cartesian coordinates, the formal solutions posed in Eq 15 are not directly integrable into closed-form expressions needed for steady-state PGBG profiles.

---

[1] The minus sign included in Eq 9 is consistent with a PGBG's positive curvature and maxima located in quadrants III and IV of the (μ,η) coordinates in Fig. 2.

724

J. Phase Equilib. Diffus. (2022) 43:718–737

$$\int_0^{\mu(\eta)} d\mu = \mu(\eta; \eta_0, \Psi) = \mp \int_{\eta_0}^{\eta} \frac{1 - 2(\eta^2 - \eta_0^2)}{\sqrt{1 - (1 - 2(\eta^2 - \eta_0^2))^2}} d\eta, \quad (\eta \leq \eta_0(\Psi) < 0).$$
(Eq 15)

2.3 Variable Transform

The range condition imposed on the profile slopes, Eq 8, applies only at each pair of triple junctions, where the slopes are $p = \pm \tan \frac{\pi - \Psi}{2}$. Starting for example at the origin, where $p = 0$, and integrating anti-clockwise, a profile's slope angle increases continuously toward its maximum value, $(\Psi - \pi)/2 > 0$, at its left-hand triple junction. Upon crossing this triple junction, the maximum slope reverses sign, whereupon it again smoothly approaches zero at the next midpoint. See Fig. 2. Thus, conditions for the midpoints, Eq 7, and for the triple-junctions, Eq 8, set an explicit cyclic limit on Eq 13, which may now be separated and integrated as,

$$\int_0^{\tan\left(\frac{\pi - \Psi}{2}\right)} \frac{dp}{\frac{1}{p}(1 + p^2)^{\frac{3}{2}}} = -4 \int_{\eta_0}^{\eta_{tj}} \eta d\eta, \quad |p| \leq \tan\left(\frac{\pi - \Psi}{2}\right).$$
(Eq 16)

In short, the combined slope conditions define the difference allowed between the squared values of a profile's limiting η-coordinates, which is compatible with its dihedral angle. This integrated "amplitude" expression establishes geometric relationships among *all* the parameters that control a PGBG's shape, including its dihedral angle, mid-point, and triple junctions. Specifically,

$$\sin \frac{\Psi}{2} = 1 - 2\left(\eta_{tj}^2 - \eta_0^2\right).$$
(Eq 17)

To verify the amplitude condition, Eq 17, we checked its asymptotic limits for *isolated* GBGs, where a profile's midpoint $\eta_0 \to 0$, and its boundary spacing $\Delta_\mu \to \infty$. If $\Psi = 0$, Eq 17 returns the lowest profile ordinate allowed for an isolated GBG as $\eta_{tj} \to -\sqrt{2}/2$. This limit agrees with the known triple-junction depth established in an earlier analysis of isolated GBGs with $\Psi = 0$.[18] GBG profiles that yielded this maximum depth were available as transcendental expressions of elementary functions given i..n[4, 9]

Equation 17 also suggests a generalization that leads to a useful transformation of variables. One notes that the *limiting* slope angles found at each triple junction location, η_{tj}—call these angles $\pm\theta_{tj}$, respectively—equal the complement of a profile's *semi-dihedral* angles: namely, $\theta_{tj} = \pm(\pi - \Psi)/2$. This of course applies only at the triple junctions. Upon further inspection, however, one also notes that an analogous relationship holds along the profile.

Specifically, one finds that the complement of *any* slope angle, $\theta(\eta)$, viz., $(\pi/2 - \theta(\eta))$, satisfies a condition analogous to Eq 17, at any profile ordinate, η.

This generalization of a profile's local slope-angle "amplitude condition", yields a cosine-transform for each semi-profile. Thus, the restricted trigonometric relationship found at the triple junctions, Eq 17, is extensible to other profile points as the variable transform,

$$\sin\left(\frac{\pi}{2} - \theta(\eta)\right) = \cos(\theta(\eta)) = 1 - 2(\eta^2 - \eta_0^2), \quad \left(\frac{\Psi - \pi}{2} \leq \theta \leq \frac{\pi - \Psi}{2}\right).$$
(Eq 18)

The cosine-transform, Eq 18, provides the correct slope anti-symmetry around each mid-point, where $\theta = 0$. Moreover, this transform converts a PGBG's metric η-integral, Eq 15, into an equivalent angular θ-integral that is at last integrable. Thus, for the second integration of a variational PGBG's ODE, using the cosine transform, one obtains

$$\int_0^{\mu(\theta)} d\mu = \pm \frac{1}{2\sqrt{2}} \int_0^{\theta} \frac{-\cos\theta}{\sqrt{1 + 2\eta_0^2 - \cos\theta}} d\theta, \quad \left(\frac{\Psi - \pi}{2} \leq \theta \leq \frac{\pi - \Psi}{2}\right).$$
(Eq 19)

As indicated in Eq 19, the definite θ-integral describes a PGBG's "profile" in terms of a slope angle function, $\mu(\theta) = \pm\Theta(\theta; \eta_0, \Psi)$. These functions have controlling parameter inputs that consist of the profile's midpoint-coordinate, $\eta_0 < 0$, and its dihedral angle, $\Psi \in (0, \pi)$. The variational $\mu(\theta)$-solution to Eq 10 now integrates into a closed form consisting of weighted, incomplete elliptic integrals in the running variable, $\theta/2$:

$$\mu(\theta; \eta_0, \Psi) = \pm \left\{ \eta_0 \text{EllipticE}\left[\frac{\theta}{2} \Big| \frac{-1}{\eta_0^2}\right] - \left(\frac{2\eta_0^2 + 1}{2\eta_0}\right) \text{EllipticF}\left[\frac{\theta}{2} \Big| \frac{-1}{\eta_0^2}\right] \right\}, \quad \left(\frac{\Psi - \pi}{2} \leq \theta \leq \frac{\pi - \Psi}{2}\right).$$
(Eq 20)

The notation adopted here for a PGBG's "θ-profile", Eq 20, is that used by Gradshteyn and Ryzhik[19]. Specifically, the functions EllipticE$[\phi|\ m]$ and EllipticF$[\phi|\ m]$ denote, respectively, incomplete elliptic integrals of the first and second kind, in Legendre form. Insofar as the nomenclature for elliptic integrals is formalized, we chose:

(1) an angular amplitude, the θ-solution's running variable, to be $\phi \equiv \theta/2$,

(2) an m-parameter, a constant related to the midpoint ordinate, as $m \equiv -1/\eta_0^2$.

With values chosen for the dihedral angle, $\Psi \in (0, \pi)$, and the midpoint coordinate, $\eta_0 < 0$, one defines the shape of a variational PGBG, and its steady-state location in (μ, θ)-space.

2.4 PGBG Metric-Profiles

Operational procedures such as differentiation, integration, and numerical evaluation of PGBG semi-profiles are all needed subsequently[2] to determine their first-order energies of formation, and to investigate their higher-order capillary-mediated thermodynamic fields. First-order energy fields and those based on higher-order interfacial gradients may be evaluated by selecting the ϕ-amplitude and m-parameter for their elliptic integral solution, Eq 20, which describe their steady-state θ-curves, but not their metric profiles.

In order to transform steady-state $\mu(\theta)$ curves into metric $\mu(\eta)$ profiles, one may cross-plot $\mu(\theta; \eta_0, \Psi)$ data sets into isometric form, $\mu(\eta; \eta_0, \Psi)$. Alternatively, and more conveniently, one may directly evaluate PGBG metric semi-profiles. The latter is accomplished by replacing the elliptic integrals' angular amplitude, $\theta/2$, in Eq 20, by its equivalent inverse, derived from the transform, Eq 18, which is $\theta = \arccos\left(1 - 2(\eta^2 - \eta_0^2)\right)$.

Tabulation of a profile's isometric coordinates, (μ, η), can be accomplished easily using the following metric formulas:

$$\pm\,\mu(\eta; \eta_0, \Psi) = \Re\left[\eta_0 \text{EllipticE}\left\{\frac{1}{2}\arccos\left[1 - 2(\eta^2 - \eta_0^2)\right], -\frac{1}{\eta_0^2}\right\}\right]$$
$$- \Re\left[\frac{(2\eta_0^2 + 1)}{2\eta_0}\text{EllipticF}\left\{\frac{1}{2}\arccos\left[1 - 2(\eta^2 - \eta_0^2)\right], -\frac{1}{\eta_0^2}\right\}\right].$$
$$\text{(Eq 21)}$$

Employing a symbolic solver, e.g., *Mathematica* ©, profile coordinates may be tabulated and plotted to high precision with these analytic formulae.

To that end, we further suggest adding $\Re[\,]$, as real-part operators, which are helpful when generating large profile data strings stripped of any extraneous null imaginary terms. PGBG metric profiles extend over a prescribed ordinate-range, viz., η_0 to η_{tj}, that depends only on the values of the dihedral angle, Ψ, and the midpoint-coordinate, η_0. A profile's triple-junction ordinate may be determined from these two shape-defining parameters by solving Eq 18 for the η_{tj}-value where their terminal slope angles equal $\theta_{tj} = \pm(\pi - \Psi)/2$.

The triple junction ordinate is determined by the choice of Ψ and η_0, as

$$\eta_{tj} = -\sqrt{\frac{1}{2} + \eta_0^2 - \frac{1}{2}\sin\left(\frac{\Psi}{2}\right)}, \quad (\eta_{tj} \leq \eta_0 \leq 0, \ 0 \leq \Psi < \pi).$$
$$\text{(Eq 22)}$$

Lastly, periodicity of PGBG profiles is achieved by translating their combined semi-profiles along the $\pm\mu$-axis by fixed increments, $\Delta_\mu \equiv \pm\lambda/2\Lambda$. The dimensionless repeated spacing, $\Delta_\mu = 2 \times \mu(\eta_{tj})$, is also determined once the parameter pair (Ψ, η_0) is selected.

2.5 Steady-State Features

A few isometric variational PGBG profiles are plotted in Fig. 3. Profiles were obtained from Eq 21, which provides the dimensionless metric solution to the variational ODE, Eq 10. The profiles selected for Fig. 3 all have the same dihedral angle, $\Psi = 0$, but display a range of shapes and triple-junction spacings that vary between about $\Delta_\mu \approx 1$ (for $\eta_0 = -0.4$) to $\Delta_\mu \approx 5$ (for $\eta_0 = -0.006$). Cusp depths, $\eta_0 - \eta_{tj}$, decrease extremely slowly with increasingly negative midpoint parameters, from their maximum allowed value of $\sqrt{2}/2$ at the asymptotic limit for PGBGs, where $\eta_0 \to 0$.

Triple junction separations, Δ_μ, are derived metrics, also determined by the choices of midpoint parameter and dihedral angle. Thus, the parameter pair (Ψ, η_0) is equivalent to selecting the grain boundary spacing and the dihedral angle when simulating PGBG microstructures. Modeling variational profiles, therefore, differs fundamentally from procedures required in phase-field simulations. In the latter case, one specifies a grain boundary spacing in a calculation box, and also chooses the energy density ratio for the s/ℓ interface and the intersecting grain boundaries. The energy density ratio chosen establishes the
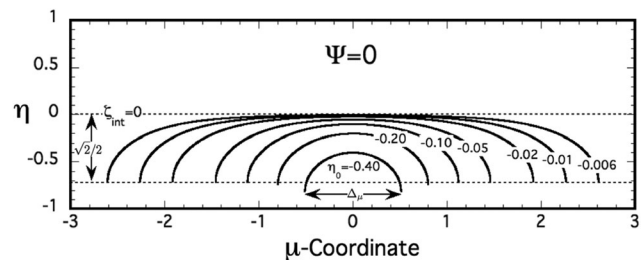
Fig. 3 Variational PGBG profiles predicted from Eq 21. Profiles are plotted isometrically in dimensionless Cartesian coordinates. Each profile is automatically positioned with respect to the system's isopotential, $\zeta_{int} = \eta = 0$, so their curvatures, $\hat{\kappa}(\mu, \eta) = -4 \times \eta$. The separation between triple junctions is set by the values of their midpoint parameter, η_0, given that these profiles all have $\Psi = 0$. The interface depression at triple junctions (the cusp depth) equals a PGBG's midpoint ordinate minus its triple-junction ordinate. Cusp depths and triple-junction spacings both decrease as midpoint parameters become increasingly negative

---

[2] A consequence of using the cosine-transform solution is that one unit of a periodic profile requires summing and plotting, separately, data from the pairs of weighted elliptic integral functions. Each pair is signed $+$ and $-$, to correspond to their left and right semi-profile, respectively.

726

J. Phase Equilib. Diffus. (2022) 43:718–737

equilibrium dihedral angle approached at steady-state. Real GBGs, of course, have all those physical conditions fulfilled by natural circumstances.

2.6 Influences of Dihedral Angle

Choosing a value for the dihedral angle implicitly selects the ratio of the grain boundary energy density to that of the s/ℓ interface. The interplay among the "natural" microstructure parameters, Ψ, and the grain boundary spacing, Δ_μ, and among the actual "variational" parameters, Ψ and η_0, are both illustrated in Fig. 4. Their combinatorial influence on the details of the resultant PGBG shapes are, however, much less obvious.

For example, profiles plotted in Fig. 4, Panel A, show representative PGBGs for several dihedral angles and a constant midpoint value, $\eta_0 = -0.05$. Although increasing the dihedral angle at constant η_0 merely exposes less and less of a profile's curved form, the increase in dihedral angle simultaneously also forces a reduction in the triple junction separation. Panel B, by contrast, illustrates PGBG profiles that maintain a fixed triple junction spacing, Δ_μ, for the same dihedral angle. Profiles with constant boundary spacing at different dihedral angles require different η_0-values, which also changes a profile's curvature and thermopotential distributions. Specifically, as η_0-values approach zero, they: 1) narrow a profile's range of curvatures; 2) shift a profile's average steady-state thermopotential toward zero; and 3) maintain the equilibrium slope value at each triple junction, as required by the dihedral angle.

2.7 Curvature Distribution

Kastner's formula from differential geometry[20] defines in-plane curvature as the arc-length derivative of the slope-angle, specifically, $\hat{\kappa} \equiv d\theta/d\hat{s}$. In 2-D, interface curvature responding to a linear thermal field also increases linearly along the gradient direction, per the Gibbs-Thomson relation. Equation 6 may be written in terms of the local slope angle, by replacing the η-variable using the cosine transform, Eq 18. This substitution permits a PGBG profile to be expressed as a function of its continuous slope-angle, $\theta(\eta)$, provided that the angles remain within its cyclic eigenrange: viz., $\frac{\Psi - \pi}{2} \leq \theta \leq \frac{\pi - \Psi}{2}$. With that restriction obeyed, and symmetry requirements applied, a PGBG's angular curvature distribution at steady-state, $\hat{\kappa}(\theta)$, becomes:

$$\hat{\kappa}(\theta) = 2^{\frac{3}{2}}\sqrt{1 + 2\eta_0^2 - \cos\theta}, \quad \left(\frac{\Psi - \pi}{2} \leq \theta \leq \frac{\pi - \Psi}{2}\right).$$
(Eq 23)

Equation 23 and its derivatives are used later, in §4, to determine arc-length distributions of the interfacial curvature and several higher-order scalar and vector field quantities that are of thermodynamic importance.

3 Energy, Stability, and Accessing Steady-State

The initial goals of this study were: (1) find an analytic expression in 2-D for variational PGBG profiles, e.g., Eqs 21 and Fig. 3; and (2) determine their curvature distributions, Eq 23. As mentioned, PGBGs form steady-state microstructures with an additional degree of freedom, namely, a variable range of grain boundary spacings. In prior theoretical analyses based on isolated GBGs, only one shape-varying parameter was available: the profile's dihedral angle.[8, 9]

Interest now centers on: (1) determining the free energy to form PGBGs, to establish their microstructure stability,
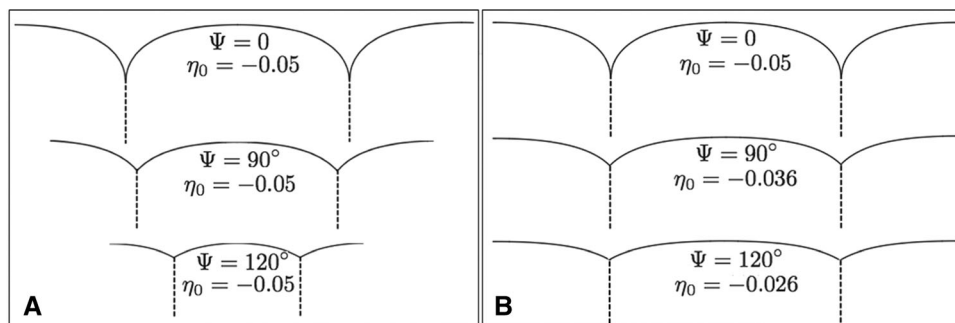

Fig. 4 Effects of increasing the dihedral angle, Ψ, on variational profiles. *Panel A*: Profiles compared at a constant midpoint undercooling and midpoint curvature, set by their *fixed* ordinate, $\eta_0 = -0.05$. Steady-state PGBG profiles with larger dihedral angles display reduced grain boundary spacings and expose less of their outer more-curved regions. *Panel B*: Profiles compared at a *fixed* grain boundary separation, Δ_μ, with increasing dihedral angles, require compensatory reductions in each profile's midpoint undercooling. Thus, η_0-values nearer zero significantly flatten the profiles

and verify access[3] to *simulated* steady-states using specified initial conditions that result in successful counterpart phase-field computations; (2) calculating gradients of the interfacial chemical potential and their higher-order divergences, the latter accessible as the surface Laplacian of the Gibbs-Thomson thermopotential. Finally, higher-order thermodynamic quantities will be compared with independent phase-field measurements on steady-state PGBG microstructures, by accessing their more realistic *diffuse s/ℓ* interfaces. These comparisons open inquiry as to how interfacial thickness affects dynamics during solidification, and stimulates subsequent pattern formation on moving s/ℓ interfaces.

3.1 Retraction by Melting

A PGBG's free energy of formation can be estimated using a *reversible* process that follows progressive melting from an initially planar s/ℓ interface, and follows its retraction toward its final form: the steady-state profile. Reversible processes, however, are clearly not involved in the case of variational profiles, because they appear *instantaneously* by solving Eq 19, which yield, *ab initio*, fully formed profiles without benefit of any initial state, or temporal development. Nevertheless, their equivalent energetic cost from a hypothetical initial state can be calculated.

First-order formation free energy provides the necessary condition required for the stability of a variational profile. It also supplies encouragement that a counterpart phase-field image, which develops from a stepwise thermodynamic sequence, would successfully approach an equivalent counterpart "evolved" steady-state, using the same periodic boundary conditions. Variational profiles and their capillary-mediated fields could then be compared quantitatively with temporally-evolved counterpart PGBGs, the latter evolved "thermodynamically" using phase-field simulation. Figure 5 suggests a schematic sequence of these virtual steps.

3.2 Free Energy Functional

The free energies associated with forming one cycle of a PGBG from a planar s/ℓ interface initially positioned along the system's x- or μ-axes are expressed as a functional. These first-order energy exchanges collectively relax the perturbed state, as the s/ℓ interface reversibly melts and retracts under localized tensions from the grain boundaries. The s/ℓ interface continuously curves, lengthens, and retracts, in the surrounding thermal field. Note that the s/ℓ
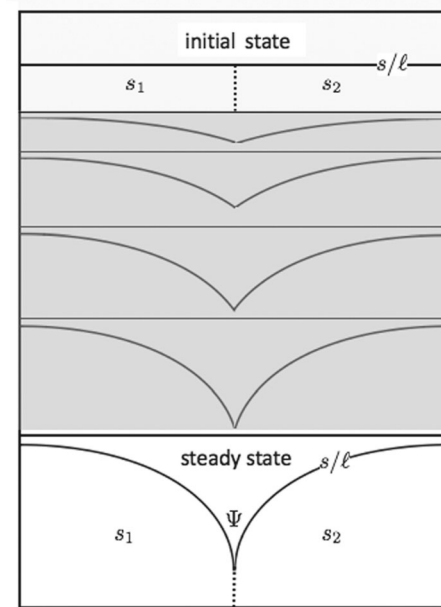
---

[3] Negative formation free energy is only a *necessary* condition for thermodynamic access to a steady-state; it does not, however, guarantee subsequent stability against perturbations.

Fig. 5 Virtual formation of a PGBG with final dihedral angle, Ψ, in a vertical thermal gradient. Panels illustrate the process of retraction by melting, with transient steps shown in gray. Each reversible step, from top-to-bottom, shows progressive interface melting and curving from its initial planar state. Retraction by melting results in shortening grain boundaries and lengthening the s/ℓ interface, until *local* thermal, chemical and mechanical equilibria are satisfied along the curved interface, and the equilibrium dihedral angle occurs at steady-state. The melt volume above the retracted interface, and below the system's melting point isotherm, becomes increasingly undercooled as the steady-state is approached. At steady-state, heat flow within the bulk phases continues to generate entropy everywhere

interface and grain boundaries extend a unit distance, $\Delta z = 1$ [m], into the 3rd dimension.

The free energy to form one repeating unit of a 3-D PGBG consists of,

(1) $E_{int} > 0$, the energy stored curving an initially flat interface between triple junctions, thereby extending the s/ℓ arc length, $s_{s\ell}(x, y)$;

(2) $E_{gb} < 0$, the energy released shortening the grain boundaries and reducing their areas, by melting back the triple junctions, as the s/ℓ interface curves, and the system acquires its equilibrium dihedral angle;

(3) $E_{cusp} > 0$, the energy required to undercool those portions of the melt volume in contact with curved solid, or otherwise positioned below the melting point isotherm.

When summed at steady-state, these energies equal the system's total free energy change, ΔE_{sys}, to form a PGBG profile, referenced to the system's initial state. The energy change to form this microstructure may be represented as the first-order functional, $F(x, y, \frac{dy}{dx}; y_0, \Psi)$ [J]. A PGBG

occupies quadrants III and IV of the (x, y)-coordinates in Fig. 1, and the (μ, η)-coordinates in Fig. 2. Inasmuch as the profile extends into the physical system's 3rd spatial dimension, z, as a 2-D manifold, each integral will be initially multiplied by the arbitrary unitary extension into the third dimension, $\Delta z = 1$[m].

A PGBG's energy functional contains four integrals, which together represent: (1) energy released by melting sectors, S_{gb}, of the grain boundary pair[4]; (2) energy stored in the profile from lengthening and curving the s/ℓ interface[5]; and (3) energy required to undercool and raise the entropy of the melt phase relative to that of the solid phase it has replaced. Only a portion of the undercooled melt volume actually contacts the curved solid, from its mid-point to its triple junctions. Additional undercooled melt that lacks contact with the solid phase is located above the profile's midpoint, at y_0, and below its melting point, at $y = 0$.

The energy functional for the formation of steady-state PGBGs from their planar initial state may be expressed, for uniformity, as four integrals in the profile's running variable, y:

$$F(x, y, \frac{dy}{dx}; y_0, \Psi) = \Delta z \int_0^{y_{tj}} \gamma_{gb}\left(\frac{dS_{gb}}{dy}\right)dy$$
$$+ 2\Delta z \int_{y_0}^{y_{tj}} \gamma_{s\ell}\left(\frac{dS_{s\ell}}{dy} - \frac{dx}{dy}\right)dy + \Delta z \int_0^{y_{tj}} \lambda(y_0, \Psi)\left(\frac{\Delta S_f G}{\Omega}\right)y\,dy$$
$$- 2\Delta z \int_{y_0}^{y_{tj}} \left(\frac{\Delta S_f G}{\Omega}\right)yx\,dy.$$

$$(Eq\ 24)$$

The first term on the right-hand side of Eq 24 equals E_{gb}, which is negative; the second term equals E_{int}, which is positive; and the last two terms sum as E_{cusp}, which is positive. The total of all terms equals the system's virtual energy change, ΔE_{sys}, to form variational profiles from their initial state. Moreover, ΔE_{sys} must remain negative to allow both spontaneous occurrence of PGBGs, and provide the necessary condition for accessing terminal steady-states if simulated thermodynamically from its initial state.

3.3 Dimensionless Functional

An intermediate functional may be formed by dividing Eq 24 by the factor $2\gamma_{s\ell} \times \Delta z$ [J/m], and evaluating its standard integrals:

$$\frac{F(x, y, \frac{dy}{dx}; y_0, \Psi)}{2\gamma_{s\ell}\Delta z} = \left(\frac{\gamma_{gb}}{2\gamma_{s\ell}}\right)\int_0^{y_{tj}} dS_{gb} + \int_{y_0}^{y_{tj}} dS_{s\ell} - x_{tj}$$
$$+ \frac{\lambda(y_0, \Psi)}{4}\left(\frac{\Delta S_f G}{\gamma_{s\ell}\Omega}\right)y_{tj}^2 - \left(\frac{\Delta S_f G}{\gamma_{s\ell}\Omega}\right)\int_{y_0}^{y_{tj}} yx\,dy.$$

$$(Eq\ 25)$$

Additional steps to represent the functional, Eq 25, in dimension-free terms are:

(1) Recognize that the coefficient of the first term on the right-hand side (the ratio of grain boundary energy to twice the s/ℓ interfacial energy) expresses Young's vector force law at the triple junctions, so $\gamma_{gb}/2\gamma_{s\ell} = \cos(\Psi/2)$.

(2) Divide through Eq 25 by twice the capillary length, 2Λ, a step that replaces both arc-length differentials, dS_{gb} and $dS_{s\ell}$ by their respective dimensionless counterparts, $d\eta$, and the arc-length differential $\sqrt{1 + (d\mu/d\eta)^2}\,d\eta$. Division by 2Λ also introduces dimension-free coordinates, $\mu = x/2\Lambda$ and $\eta = y/2\Lambda$, into the third and fifth terms, and replaces the physical grain boundary spacing, λ, in term four, by the equivalent dimensionless separation between triple junctions, $\Delta_\mu \equiv \lambda/2\Lambda$.

(3) Finally, Eq 1 shows that the system parameters grouped in parenthesis in both terms four and five equal $1/\Lambda^2$, which substitution renders dimensionless. The remaining terms require inserting unit factors of 4/4 to complete their non-dimensionalization.

Applying all these steps yields the dimensionless functional, $\mathcal{F}(\eta, \mu, \frac{d\eta}{d\mu}; y_0, \Psi)$, to form one unit of a PGBG's (μ, η)-profile from its initial planar state:

$$\mathcal{F}(\mu, \eta, \frac{d\eta}{d\mu}; \eta_0, \Psi) = \cos\left(\frac{\Psi}{2}\right)\eta_{tj} + \int_{\eta_0}^{\eta_{tj}} \sqrt{1 + (d\mu/d\eta)^2}\,d\eta$$
$$- \mu_{tj}(\eta_0, \Psi) + \Delta_\mu \eta_{tj}^2 - 4\int_{\eta_0}^{\eta_{tj}} \mu\eta\,d\eta.$$

$$(Eq\ 26)$$

In summary, the system's non-dimensional energy change, ΔE_{sys}, to create one cycle of a PGBG microstructure from the initial system configuration consists of:

(1) Energy to lengthen the s/ℓ interface, $E_{int} = \int_{\eta_0}^{\eta_{tj}} \sqrt{1 + (d\mu/d\eta)^2}\,d\eta - \mu_{tj}(\eta_0, \Psi)$

---

[4] Only half of the grain boundary energy, γ_{gb}, lost to melting is attributed to each member of a grain boundary pair, with the remainder contributed to the immediately adjacent profile units.

[5] The s/ℓ interface has *zero* thickness, and thus lacks elastic stiffness to the imposed shape deformation from its initial planar configuration. Consequently, additional strain energies are neither stored from elastic stretching nor from bending; only energy associated with increased interfacial area is included.
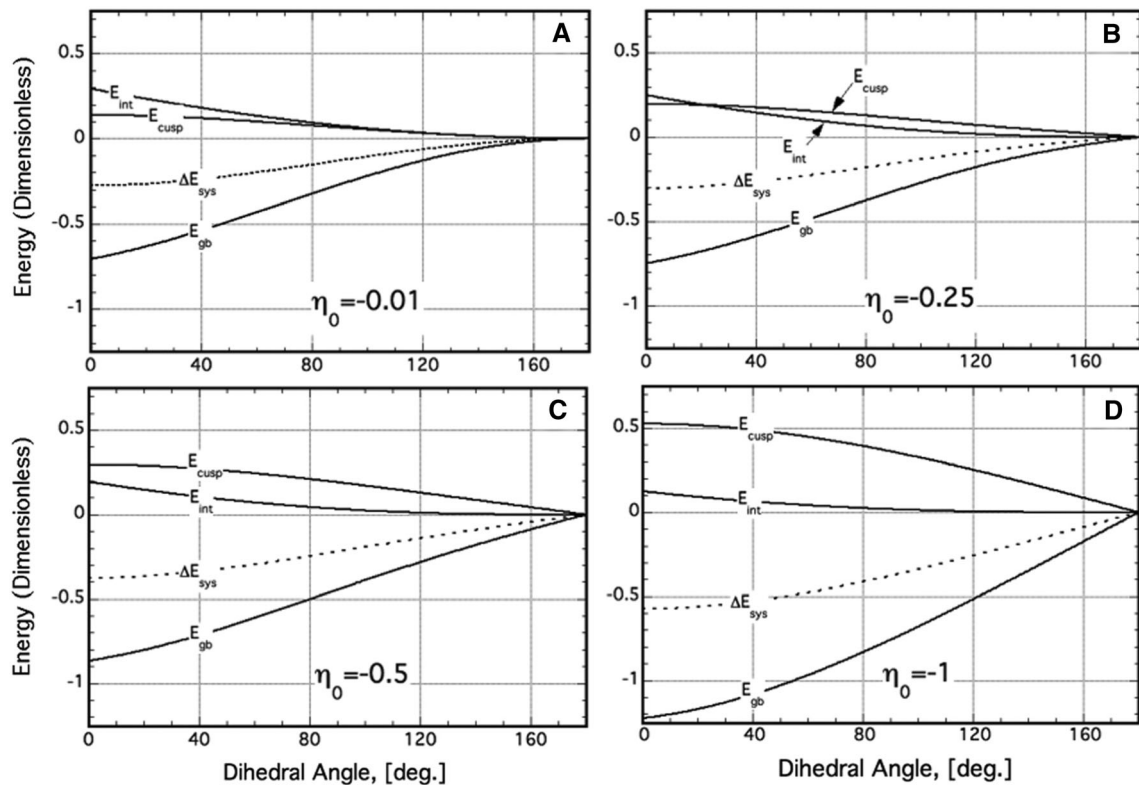
Fig. 6 Component free energies to form PGBGs versus dihedral angle (solid curves). The midpoint parameter, η_0, assigned to each panel produces markedly different steady-state microstructures. **Panel A**: The total free energy change, ΔE_{sys}, (broken curve) for *all* dihedral angles remains everywhere negative (i.e., within the necessary condition for steady-state stability, where $\Delta E_{sys} \leq 0$. **Panel B**: For $\eta_0 = -0.25$, one notes that E_{cusp} becomes greater than E_{int} where the dihedral angle exceeds about 20°. This, and subsequent panels, show that the free energy to supercool the adjacent melt is relatively sensitive to a PGBG's midpoint parameter, whereas the energies to curve and lengthen the s/ℓ interface are small and decrease gradually as η_0 becomes more negative. **Panel C**: At a midpoint value near $\eta_0 \approx -0.5$, the system's formation energy decreases almost linearly with increasing dihedral angle. **Panel D**: At more negative midpoint values, two robust processes dominate the system's formation energy: 1) undercooling the melt, $E_{cusp} \gg 0$, and 2) shortening, by retraction melting, the grain boundaries $E_{gb} \ll 0$. Lengthening the s/ℓ interface contributes moderate positive energy changes that diminish as midpoint values become increasingly negative. First-order formation energies for PGBGs, however, *always* remain negative

(2) Volume energy to undercool the melt, $E_{cusp} = \Delta_\mu \eta_{tj}^2 - 4\int_{\eta_0}^{\eta_{tj}} \mu\eta\, d\eta$

(3) Energy released from partially melting the grain boundaries, $E_{gb} = \cos\left(\frac{\Psi}{2}\right)\eta_{tj}$

3.4 Steady-State

Dimensionless energy changes to form PGBGs were calculated with the energy components listed above, along with their algebraic sum, ΔE_{sys}. Component energies are plotted in Fig. 6 as functions of a PGBG's dihedral angle, Ψ, for several values of their midpoint parameter, η_0. These plots cover a wide range of PGBG microstructures, as suggested by their profile variations in Fig. 3.

Energy changes for the formation of PGBGs remain negative at all dihedral angles and self-consistent midpoints, supporting the stability of variational profiles. This result suggested that counterpart phase-field simulations of PGBGs would likely also converge to stable steady-states when simulated using phase-field methods.

We note that an earlier study of the thermodynamics of *isolated* GBGs,[18] which have microstructures equivalent to PGBGs in the limit of $\eta_0 \to 0$, had confirmed their steady-state stability, a fact which is both well-known and widely experimentally observed. The additional positive free energy needed to undercool the larger melt volume of PGBGs increases substantially as η_0 becomes more negative. Even this large positive term apparently never causes ΔE_{sys} to exceed zero, and lose formation stability. The energy provided by deeply retracted grain boundaries more than compensates the extra free energy to undercool the increased melt volume.

730

J. Phase Equilib. Diffus. (2022) 43:718–737

To convert the dimensionless energies given in Eq 26 and Fig. 6 back into Joules, one multiplies their dimensionless values by $4\gamma_{s\ell}\Lambda \times 1[\text{m}]$ [J], which is the capillary energy stored in a narrow strip of s/ℓ interface, with an area equal to $4\Lambda \times 1$ [m²]. Insofar as the thermocapillary scale, Λ [m], is itself proportional to $1/\sqrt{G}$, the energy that this area of interface would store is 1-10 [μJ] for most materials that form PGBGs under moderate thermal gradients, e.g.,1000 [K/m]). That estimate increases to 10-100 [μJ] for PGBGs under smaller thermal gradients, e.g., (e.g., 10 [K/m]).[21, 22] The formation free energy of a unit profile of a PGBG clearly increases as the applied thermal gradient decreases, and the physical size of the microstructure increases.

4 Higher-Order Capillary Fields

4.1 Approach

In brief, our approach to interpreting interfacial capillary effects uses paired sharp and diffuse interfaces found in one-component steady-state PGBG systems. These pairings exhibit metrically proportional profiles. Paired profiles, structured as counterpart sharp and diffuse interfaces, have proportionate distributions of both their curvatures and chemical potentials, the latter reflecting local phase equilibria via the Gibbs-Thomson effect. These similarities can be extended mathematically a step higher, by using the fact that variational profiles and their counterpart simulated PGBG microstructures also support proportionate divergences of their vector potential gradients. Field theory also shows that the surface Laplacian—a 4th-order quantity based on an interface's scaled distribution of curvatures or chemical potentials—equals the divergence of the dimensionless gradient of those quantities. Surface Laplacians of this nature have, however, received limited study in interfacial thermodynamics, despite the implication of their affecting energy and solute balances on interfaces.

It is the transition structure between bulk phases that physically allows, or prevents, tangential interface conductance, which, in turn, controls the intensities of interfacial heating and cooling, or for alloys, solute release and absorption.[23] Variational interfaces lack tangential conductance, and, consequently, do not support tangential fluxes of energy or solute as kinetic responses to the thermochemical gradients encountered along curved interfaces. Knowing an interface's *exact* shape, however, permits determination of its thermochemical gradient and surface Laplacian.

Although the shapes of simulated diffuse-interface PGBGs are known only approximately, their imputed scaled cooling rates can still be found by using the surface Laplacian of their counterpart variational profiles that bear (proportional) profiles. This scheme allows estimation of the flux divergences on steady-state diffuse interfaces, limited, however, by uncertainties of their tangential conductance. Thus, scaled cooling rates on curved diffuse interfaces can be estimated and measured *in situ* with numerical simulation. Eventually, by using experiments performed on real s/ℓ interfaces, capillary-mediated cooling rates will be measured and critically compared with this theory.

Comparative studies of proportionately curved sharp and diffuse interfaces demonstrate next that the vector divergences of their chemical potential gradient fields evoke profoundly different kinetic responses. Our approach again explains why. The scalar divergences of the potential gradients along curved interfaces can be significant, but *only* on diffuse interfaces, as they, and they alone, possess interfacial transition thicknesses that allow cooling to occur. Tangential fluxes of energy on diffuse interfaces—more specifically the flux distribution's higher-order scalar divergences—act as local energy sinks, i.e., cooling sites. Capillary-mediated sinks, in turn, modify an interface's energy balance, and depress its local thermochemical potential. This elicits measurable interfacial effects, whether interfaces are stationary, as are PGBGs, or moving during solidification. In addition, comparison of the surface Laplacian of variational PGBGs with local interface potentials and cooling rates on simulated diffuse microstructures, identifies their thermodynamic origin and suggests seeking control methods.

The connections described above between the correlated thermodynamic behavior of sharp and diffuse interfaces with proportionate curvature distributions was first demonstrated with isolated GBGs.[8, 9] Recently those connections were extended by the present authors to PGBGs.[24] Derivation of PGBG profiles from variational theory, theoretical assessment of their thermodynamic stability, and now simulated measurements compared with the surface Laplacian, are interesting and extremely suggestive. They do not as yet provide definitive proof of their effect on real interfaces during crystal growth, as will critical experiments to be performed in the future.

4.2 Surface Laplacian

The mathematical methods applied in Section 2 to develop expressions for variational profiles of PGBGs implicitly required that their interfaces represent: 1) abrupt structural changes between locally equilibrated phases, and 2) s/ℓ interfaces that are isotropic, i.e., $\gamma_{s\ell} =$ const. With these restrictions satisfied by variational PGBGs, one may apply

the following ODE to calculate the surface tangential τ-Laplacian of the Gibbs-Thomson thermopotential[7, 18]:

$$\nabla_\tau^2[\zeta_{int}(\theta)] = \hat{\kappa}_{\theta\theta}\ \hat{\kappa}^2(\theta) + \hat{\kappa}_\theta^2\ \hat{\kappa}(\theta). \qquad (Eq\ 27)$$

Equation 27, derives from interfacial field theory and is of purely geometric origin. Substituting the non-dimensional profile curvature distribution, $\hat{\kappa}(\theta)$, Eq 23, into the right-hand side of Eq 27, along with its scaled angular derivatives, $\hat{\kappa}_\theta$ and $\hat{\kappa}_{\theta\theta}$, yields the divergence of the vector gradient of the thermopotential, or, equivalently, the surface Laplacian of the interface's $\zeta_{int}(\theta)$-potential. Thus, simulated and real interfaces with proportional curvature distributions can be metrically scaled into profiles with identical surface Laplacians as their variational counterparts. This is the essential idea of using geometric homology to conduct proportionate comparative thermodynamic analyses.

More specifically, the surface Laplacian is the 2-D operator that Jackson defines as "the flux density of the implied gradient flow".[25] This operator is 4th-order with respect to an interface's shape, and 2nd-order with respect to its curvature. Most importantly, however, the surface Laplacian along a variational PGBG's s/ℓ interface manifests itself physically as the following angular distribution of scaled cooling rates:

$$\nabla_\tau^2[\zeta_{int}(\theta)] = 2^{\frac{7}{2}}\cos\theta\sqrt{1 + 2\eta_0^2 - \cos\theta}, \quad \left(-\frac{\Psi}{2} \le \theta \le \frac{\Psi}{2}\right). \qquad (Eq\ 28)$$

Equation 28, describes the exact angular distribution of the divergence of a *variational* PGBG's dimensionless Gibbs-Thomson gradients, which are proportionate to measurable residuals of the thermopotential (and the local interfacial cooling rate) along a *simulated* PGBG. Thus, we found that simulated steady-state microstructures can provide proportionate gradient structures with measurable flux divergences, or cooling rates.

We summarize this chain of logic for a one-component system: a positive surface Laplacian implies divergence of heat flow, i.e., removal of energy, which locally cools a s/ℓ interface. Alternatively, a negative surface Laplacian implies convergence of the thermal gradient field, i.e., concentration of heat energy, which locally warms a s/ℓ interface. In either event, the local interfacial energy balance is affected by capillarity-mediated fluxes. These divergent interfacial heat fluxes are assumed to be stimulated as described by Fourier's heat equation, as a linear 1-D tangential vector field responding to tangential thermal gradients induced by curvature.
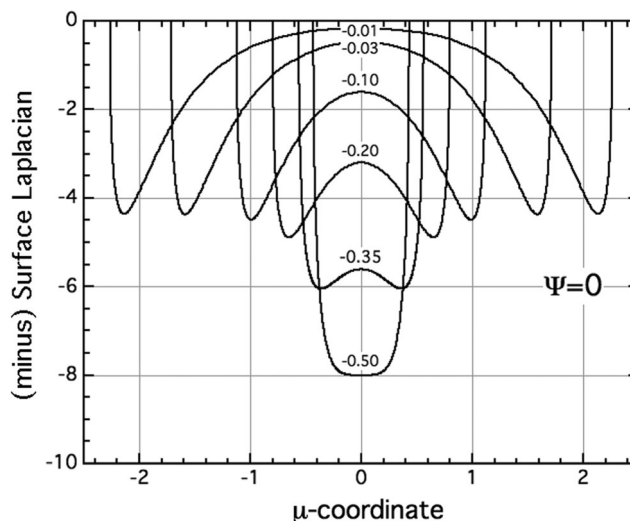

Fig. 7 Minus the surface Laplacian of the thermopotential, $-\nabla_\tau^2[\zeta_{int}(\mu)]$, calculated with Eq 28 for different PGBGs, and then cross-plotted against the μ-coordinate of their profiles using Eq 20. These distributions show divergences of the implied flux density, i.e., cooling of the interface, in *all* cases. One sees that PGBGs with relatively wide grain boundary spacings, such as those labeled $\eta_0 \ge -0.35$, exhibit Laplacians that display pairs of extrema with cooling rates between about -4 and -6. Narrower boundary spacings, $\eta_0 \le -0.4$, display only a single extremum centered at the midpoint

4.3 Distribution of Divergences

Distributions of the surface Laplacian of the Gibbs-Thomson thermopotential, $-\nabla_\tau^2[\zeta_{int}(\mu)]$, were obtained by cross-plotting (minus) Eq 28 against a profile's, $\mu(\theta)$-coordinate. The Laplacian distributions in Fig. 7 show expected changes in the *implied* density of the Gibbs-Thomson gradient flow for several values of a PGBG's parameters. (See again Fig. 3 for the relationships among the PGBG's parameter pair, (η_0, Ψ), its profile, and grain boundary spacing, Δ_μ.) In all the cases of PGBGs simulated at steady state, only positive surface Laplacians occurred. Positive Laplacians represent positive divergences, or implied gradient-*outflow*, which cause a distribution of steady-state cooling rates over the s/ℓ microstructure.

Depending on the grain boundary spacing, both single and double cooling extrema appear centered about each profile's midpoint. For η_0-values closer to zero, the grain boundary spacings increase to $\Delta_\mu \approx 5$, which could increase without limit as $\eta_0 \to 0$. By contrast, as η_0-values become more negative, from about -0.2 to -0.5 and beyond, grain boundary spacings contract, and interface cooling rates strengthen sharply. These tendencies reflect an underlying subtle conservation condition for capillary cooling, to be explained in Sect. 5.

Quantitative changes in the predicted cooling rate distributions illustrated in Fig. 7, as well as qualitative cooling

distributions that appear on simulated microstructure thermal maps in Fig. 10, both suggest that the surface Laplacians of the Gibbs-Thomson thermopotential for PGBGs depends sensitively on their shape, especially their triple-junction spacing and curvature distribution. Accordingly, capillary cooling fields also change strongly with their paired profile parameters, η_0 and Ψ, as well, of course, with the system's material and thermal properties outlined in Sect. 1.2.

4.4 Integrated "Cyclic Divergence"

Now that distributions of the gradient divergence are available from Eq 28, and their influences on the thermal maps confirmed, it is of interest to calculate the integrated divergence of the potential gradient over one full PGBG cycle. This yields a "global" cooling rate for a diffuse microstructure that equals the steady-state overall rate of energy extraction over one s/ℓ unit profile. This energy is continually absorbed at locally different rates by divergent tangential heat currents driven along the interface.

Equation 27, which defines the surface Laplacian, may be rearranged by dividing through by the interface curvature, and applying Kastner's formula to introduce differentials of the arc length, $d\hat{s}$, and slope angle, $d\theta$. These steps allow the variables in Eq 29 to be separated and integrated over the entire profile:

$$\frac{\nabla_\tau^2[\zeta(\theta)]}{\hat{\kappa}(\theta)} = \nabla_\tau^2[\zeta_{int}(\theta)]\left(\frac{d\hat{s}}{d\theta}\right) = -\left(\hat{\kappa}_{\theta\theta}\ \hat{\kappa}(\theta) + \hat{\kappa}_\theta^2\right).$$
(Eq 29)

The line integral of the surface Laplacian of the ζ_{int}-potential over one cycle of a PGBG equals the global interfacial cooling, which is the total rate of energy conducted from the surrounding bulk phases and absorbed by the stationary diffuse s/ℓ interface:

$$\oint \nabla_\tau^2[\zeta_{int}(\theta)]d\hat{s} = 2\int_0^{\frac{\pi-\Psi}{2}}\left(\hat{\kappa}_{\theta\theta}\ \hat{\kappa}(\theta) + \hat{\kappa}_\theta^2\right)d\theta. \quad \text{(Eq 30)}$$

Inserting the curvature function of a PGBG profile, $\hat{\kappa}(\theta)$, Eq 23, along with its first two angular derivatives into Eq 30 yields after integration, and considerable simplification, a surprising result: the global cooling rate per cyclic unit of the interface depends only on a PGBG's dihedral angle; the midpoint parameter, η_0, cancels out of the summed integrands on the right-hand side of Eq 30. One then finds,

$$\oint \nabla_\tau^2[\zeta_{int}(\theta)]d\hat{s} = -8\int_0^{\frac{\pi-\Psi}{2}}\cos\theta\ d\theta = -8\cos\frac{\Psi}{2}.$$
(Eq 31)

For the dihedral angle $\Psi = 0$, a PGBG's unit cyclic line integral of its surface Laplacian distribution equals -8.

(Compare Fig. 7, where markedly different Laplacian distributions, with $\Psi = 0$, are now found to conduct the same total amount of energy per unit time from their surroundings.) This result is a global interface conservation condition that depends solely on a PGBG's dihedral angle. As illustrated in Fig. 3, a PGBG's shape depends sensitively on its midpoint parameter, η_0, as does its curvature distribution. Despite markedly different capillary-mediated cooling-rate distributions, their integrated rate of interfacial energy absorption per cyclic unit is $-8\cos\frac{\Psi}{2}$. Equation 31 generalizes the previously reported value of -8, for the integrated cooling rate of an *isolated* GBG microstructure with $\eta_0 \to 0$, and $\Psi = 0$.[18]

5 Phase-Field Simulation

Phase-field simulation, in the present context, determines the temporal and spatial aspects of a system's phase-indices, which are local time-dependent functions designated $\phi[n]_{i,j}$. The phase-index subscripts (i, j) designate the discrete square sub-areas into which the entire system is subdivided within a *single* computational domain. Individually computed squares undergo stepwise changes of their phase state. Phase indices, in a sense, are thermodynamically computed "avatars" that stand for the relative presence $(\phi[n]_{i,j} \to 1)$, or absence $(\phi[n]_{i,j} \to 0)$, of a phase, n, in square (i, j), at each computational time step. The phase-indices represent a pure crystalline phase, $[n] = 0$ and $[n] = 1$, that differ only in their spatial orientations, whereas phase index $[n] = 2$ represents their common melt phase. A multiphase-field model is thereby required.

The system's initial condition is shown in Fig. 8. All bulk-phase regions consist of single component phases. Intermediate values of a phase-index argument, viz., $0 < \phi[n]_{i,j} < 1$, model higher energy "intermediate" states, required at each phase and grain boundary transition. To reach steady-state under the imposed thermal and symmetry constraints, the system's overall free energy is steadily minimized over time to form a microstructure of bulk solid and liquid domains, contoured and separated by s/ℓ surfaces and grain boundaries. What is truly notable about phase-field models is that they use only a single overall computational domain: this essential feature avoids the difficult task of tracking moving phase boundaries. Even so, phase-field fully supports the occurrence of realistic topological events during phase change. These include nucleation, pinch-off, particle disappearance, and, what is most critical for this study, diffuse phase transitions, where thermodynamic fields, such as potentials, gradients, fluxes, and their divergences can be measured *in situ*. Multiphase-field equations and their parameters, as
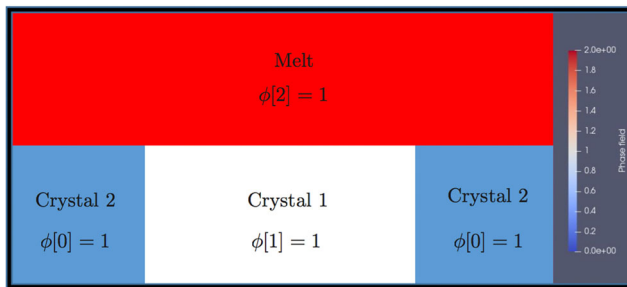
J. Phase Equilib. Diffus. (2022) 43:718–737

733

Fig. 8 Computation box for PGBG simulations in its initial condition. When allowed to evolve to steady-state, this initial phase configuration reverts to the phase arrangement depicted in Fig. 2 and computed in Fig. 10. Each initial subregion of the computational box starts with a bulk phase, signified by its unitary phase index, name, and color: $\phi[0] = 1$ crystal-1, blue; $\phi[1] = 1$ crystal-2, white; $\phi[2] = 1$ melt, red. The remaining two other phase indices in each *initial* subregion must be zero. Moreover, phases crystal-1 and crystal-2 are identical solid phases that differ only in their spatial orientations. They initially form subregion boundaries 0/1, blue-white, a vertical grain boundary, and 1/0, white-blue, vertical grain boundary, whereas subregion boundaries 0/2, blue-red, and 1/2, white-red are horizontal, planar s/ℓ interfaces. This initial state has, perforce, an unstable dihedral angle, $\Psi = \pi$ that at steady-state relaxes to the equilibrium dihedral angle. An upward pointing thermal gradient is applied to this system, with a heat source located at the top, with a "temperature" of 1.0 above the melting point, and a heat sink at the bottom, with a lower "temperature" of 0.98 below the melting point. Periodic boundary conditions (reflection symmetry) apply at each outer vertical boundary, and at the internal vertical "grain boundaries" (Color figure online)

well as other computational details used in our simulations, may be obtained from the authors and prior publications.[8, 9]

5.1 Sharp and Diffuse Interfaces

At steady-state, for example, so-called "isoline contours" partition different phases, and separate them by thin, but continuous transitions, which link discretely computed phase indices and approximate them as continuous curves. These diffuse s/ℓ interfaces separate bulk-solids from bulk liquid, and form diffuse grain boundaries that separate crystals 1 and 2 with their different spatial orientations. Phase borders, or isolines, join to identify contours that define spatial phase distributions and their shapes that collectively represent the evolved steady-state microstructure. Gradient divergences of the chemical potentials along these isolines, discussed earlier in Sect. 4.2, can, in principle, slightly alter these contour shapes and affect their subsequent local chemical potential, and, if a microstructure was set in motion, modify its kinetics.

Important practical questions surrounding this subject, yet to be addressed by experiments or additional simulations, ask to what extent are microstructures and their

kinetic behavior actually changed by capillarity in *specific* systems, and can these interactions be controlled? For example, interfacial stability during solidification and crystal growth are important processing issues, as are the practical effect of coarsening rates of solidifying microstructures. Phase coarsening rates depend primarily on longer-range spatial gradients of interfacial chemical potentials, as well as on higher-order capillary effects from tangential flux divergences that influence both these potentials and interface shapes. Although doubtless present, such phenomena have not yet been isolated and studied. Moreover, at present we could not resolve any resultant shape changes, per se, attributed to capillary-mediated potential shifts, because of the limited phase-field resolution currently at our disposal.

Already demonstrated in references,[8, 9] and to be compared in Sect. 5.3, the emergent profiles of sharp-interface variational profiles (yellow curves in Fig. 10, added to upper panels) closely approximate the shapes of simulated steady-state PGBG microstructures with diffuse interfaces. Close agreement between GBG theory and experiment also include many groove microstructures that have been reported and measured in energy experiments conducted on weakly anisotropic, one-component crystalline materials,[14, 15, 21, 26–28] on alloys,[29, 30] and even on colloidal substances.[31]

5.2 Residuals and Proportionality

Residuals are post-processed measurements of the change of temperature, or thermopotential, with depth along simulated steady-state s/ℓ interfaces. Thermopotential depressions are proportionate to the cooling rate applied locally by capillarity to the interface, a straightforward inference drawn from classical thermometrics, using small temperature responses from cooling a substance at steady-state. Temperature responses vary *linearly* with local cooling or heating rates, respectively, because the heat capacity of the phases comprising the s/ℓ interface remains constant for tiny temperature changes.

The critical question concerning our approach to comparative analysis, however, is whether or not the measured depression of the thermopotential along a simulated interface is also proportionate to the *thickness* of the interface and its implied thermal conductance. We verified this subtle, but critical, aspect of the phase-field model by measuring steady-state residuals data on eight different simulated groove profiles, all with the same dihedral angle. The number of pixels for the somewhat exaggerated phase-field s/ℓ isoline transitions was varied between a minimum of 8 pixels to a maximum of 24 pixels, which should change the interface's 2-D tangential conductance (W/K)
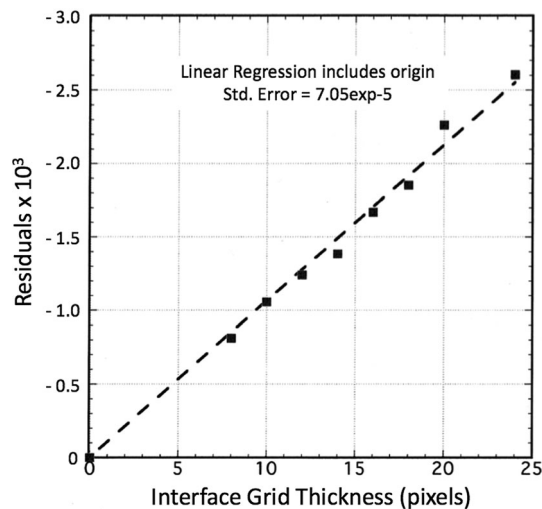
734

J. Phase Equilib. Diffus. (2022) 43:718–737

Fig. 9 The influence of interfacial isoline thickness (pixels) on capillary cooling rates and their proportionate residuals, measured on s/ℓ interfaces of simulated steady-state GBGs. The regression of eight numerical experiments shows linear behavior between the model's admittedly exaggerated interface thicknesses and the magnitudes of its measured residuals or cooling rates. Statistical analysis yields a standard error of less than 10^{-4}, even when the origin (zero interface thickness and zero residuals) was included in the regression analysis. These data are consistent with our hypothesis that thermal conductances and cooling rates of *simulated* interfaces decrease steadily with their isoline thickness, without encountering a critical minimum thickness below which cooling ceases. We stress, this correlation does not constitute proof that real s/ℓ interfaces, perhaps only a few molecular diameters wide, will likewise experience proportional cooling rates. The data show proportionate behavior between residuals, cooling rates, and interface thicknesses, consistent within the limitations of the phase-field simulations that were used at steady-state to check capillary field theory

also by a factor of 3. Accessing a still larger dynamic range for this test would require enhanced computational power.

Figure 9 shows the results of our initial "interface thickness" proportionality test of the model. Adding in the theoretical *ansatz* that cooling must vanish in the limit of zero interfacial thickness, the test of the phase-field model still showed linear regularity of interfacial thickness, magnitude of the potential residuals, and cooling rates, all in concert with our theoretical assumptions for using comparative analysis.

5.3 Steady-State

The distribution of isoline residuals and cooling rates were measured with a post-processing algorithm designed to detect and read the isoline potentials of steady-state phase-field images. Simulated images achieved steady-state after several hundred thousand calculation steps. Steady-states were always validated with cross checks of the actual dihedral angle developed at the simulated triple junctions

against their intended input values. Specifically, dihedral angle values were based on the input ratios of the grain boundary energy density to that for the s/ℓ interface. We also found that isoline potentials, once steady-state was achieved, could be measured to an accuracy of about one part in 10^4.

Simulations were visualized with their steady-state isotherm distributions, displayed here as thermal maps shown on the upper row of Fig. 10. Figure 10 also provides comparisons between surface Laplacians calculated for two variational profiles and their counterpart post-processed simulated residuals.

The algorithm to measure residuals subtracts from the measured local s/ℓ isoline potential the known linear potential distribution imposed on the microstructure by the macro-gradient. Thus, residuals data consist of post-processed isoline "temperatures", less the linear temperature distribution, and their X-grid coordinates from the simulation box. Residuals data were then multiplied by two independent scale factors: one matched the maximum vertical spread of residuals to the variation of cooling rates around the Laplacian's central value; the second scale factor just adjusted the residual's arbitrary X-grid spread to match their Laplacians' μ-axes scale. These scaled residuals were added onto the plots of their corresponding surface Laplacians. They show comparison of measured simulated cooling rates—the residuals—to interfacial cooling rates predicted from field theory. For additional details regarding residuals measurement see.[8, 9]

Note that the right-hand panels in Fig. 10 display cooling distributions with nearly twice the dimensionless triple-junction separation, Δ_μ, than is displayed on the left-hand panels. The separations, Δ_μ, indicate how remote are the most intensely cooled locations, despite each simulation having identical X-grid separations. It is the difference in the μ-axis separation of their most intensely cooled regions that explains the qualitative appearances of the cooler "blue areas" shown in the upper row. The capillary cooling distribution on the left-hand panels shows a significant, nearly uniform spread across the entire microstructure, with the very coolest regions surrounding the triple junctions. Indeed, the corresponding surface Laplacian shown below indicates nearly uniform cooling rates, between -4.5 to -5.5, extending from the midpoints toward their triple junctions. By comparison, the right-hand panel shows localized cooling, much more tightly concentrated about each triple junction, and rather weak cooling surrounding its midpoints. The corresponding surface Laplacian plotted below consistently indicates that cooling rates varied considerably, from -2.6 to -4.5, between midpoints and triple junctions.
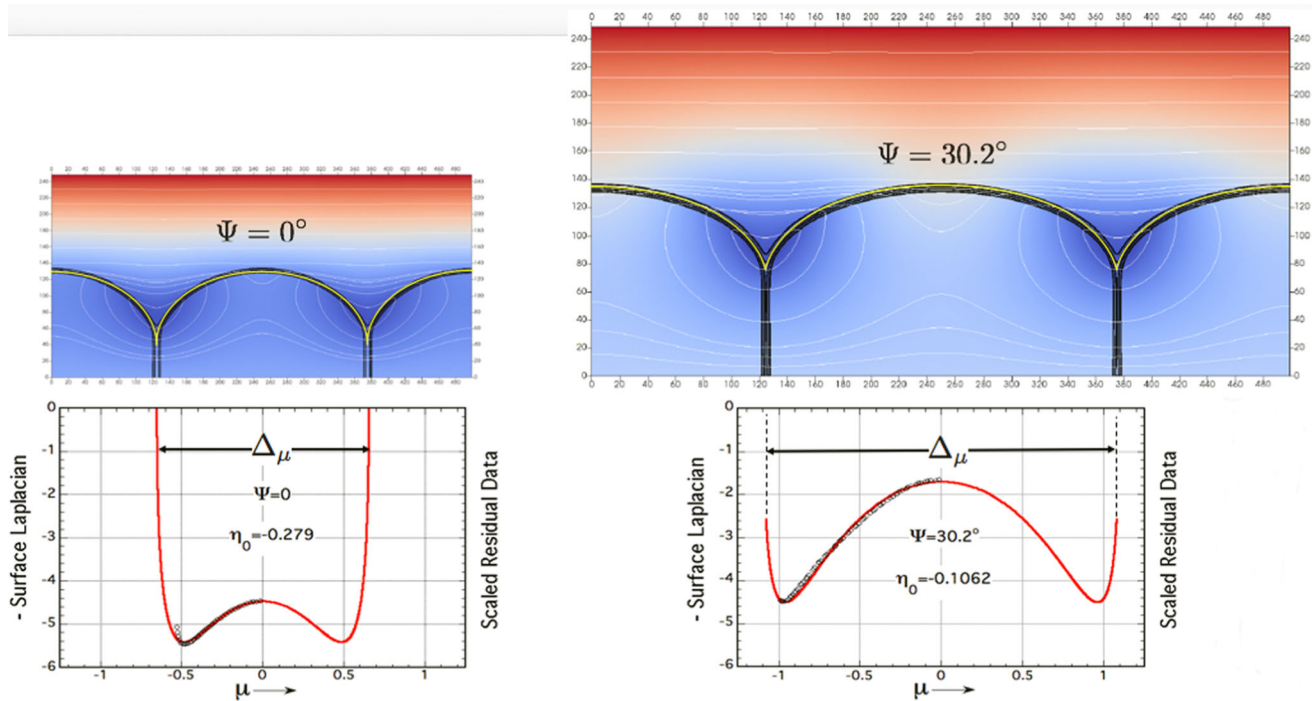
Fig. 10 Scaled comparisons of simulated isotherm maps, counterpart variational surface Laplacians, and measured potential residuals. **Upper Row**: Phase-field isotherm maps for two steady-state PGBGs. Red is warmer; blue is cooler. Maps from each simulation were adjusted isometrically to match their simulated X-grid grain boundary spacings with dimensionless triple junction separations, Δ_μ, as plotted on the lower row. Again, yellow curves added onto these simulated maps exhibit their counterpart variational profiles. Variational profiles were independently calculated from Eq 21 using matched values of

$\Psi = 0$ and $\Psi = 30.2°$, respectively, finding iterated values of η_0 that provide a $\pm 0.5\%$ match with their phase-field image's simulated aspect ratio. **Lower Row**: Surface Laplacians from Eq 28 are cross-plotted on identical μ-scales to predict isoline cooling distributions. Data points added to each Laplacian curve are measurements of simulated scaled residuals. Residuals data were measured from simulations; surface Laplacians were calculated from field theory. Each is proportional to cooling rates developed by capillarity that influence the microstructure's local temperature

Comparisons between upper and lower rows in Fig. 10 confirm that the surface Laplacian distributions predict the major qualitative features observed on the simulated thermal maps. These data specifically confirm agreement between residuals and their corresponding Laplacians, and the simulated cooling trends represented by the microstructure's steady-state thermal maps.

6 Conclusions

(1)   The analytic description of s/ℓ PGBG profiles is derived with variational theory. Mathematical description of these emergent profiles allows application of standard field theory to evaluate their interfacial scalar and vector capillary-mediated fields. These include 1st-order formation free energies from a specified initial state, as well as higher-order capillary-mediated effects, including the interfacial thermochemical potential, its gradient field, heat flux, and divergence.

(2)   1st-order formation free energies of PGBGs provide the necessary condition indicating that PGBGs develop conditionally stable structures at arbitrary grain boundary separations and dihedral angles. These results suggest that PGBGs form spontaneously during polycrystalline solidification. Their stability, moreover, is such that phase-field simulations, if initiated from appropriate configurations and simulated for a sufficiently large number of time steps, should access their terminal steady-states. Simulations obtained in the course of this study did, in fact, successfully settle into predicted steady states. Hundreds of thousands of computational steps, however, were needed to simulate PGBG phase-field profiles with sufficient accuracy to exhibit their equilibrium dihedral angles to a precision better than $\pm 0.05\%$.

(3)   Simulated s/ℓ microstructures that share identical dihedral angles with their counterpart variational PGBGs develop proportional curvature distributions. After isometric scaling, simulated PGBGs exhibit gradients of their chemical potentials with scalar flux

divergences that closely match the surface Laplacians of their variational counterparts. Thus, we confirm that phase-field simulated s/ℓ microstructures "behave" as though they support *active*, thermodynamically necessary, energy fields, as identified and assessed from their variational forms using field theory.

(4) The surface Laplacian of the thermochemical potential distribution on a variational profile is found to be *proportionate* to the cooling rates measured on its counterpart diffuse-interface PGBG. Cooling effects measured as residuals, post-processed on simulated steady-state microstructures, confirm this proportionality.

(5) Deterministic capillary-mediated energy sinks, albeit remain theoretically-based concepts. Energy sinks were detected in numerical "experiments" as interfacial cooling rates measured with precision multi-phase-field techniques. Interfacial cooling and heating from capillarity—as indirect effects arising from high-order energy sources—are not yet considered in current crystal growth dynamics, despite Turing's now famous 70-year old conjecture that simple chemical diffusion/reaction and thermal conduction, guided by appropriate geometric factors, often self-organize and instigate complex structure formation.[32] Capillary-mediated cooling and heating of s/ℓ interfaces are fourth-order phenomena, and, as such, are not included in Stefan energy or solute balances. They must, nonetheless, be taken into account when considering interface stability, especially on curved s/ℓ interfaces in low-noise environments, where small deterministic perturbations become significant.

In closing, we emphasize that when finally addressed experimentally, similar agreement might be found for the physical presence of deterministic capillary-mediated sinks and sources on real s/ℓ interfaces. Were that to happen, it should bring closer practicable manipulation of these subtle deterministic phenomena for improvement of solidification processing, welding, and crystal growth.

References

1. P. Martin, *Thermal Grooving by Surface Diffusion: Mullins Revisited and Extended to Multiple Grooves*, Quarterly J. of Applied Mathematics LXVII (2009), pp. 125–136
2. W. Mullins, Theory of Thermal Grooving. J. Appl. Physics **28**, 333–339 (1957)
3. M. Gurtin, *Thermomechanics of Evolving Phase Boundaries in the Plane, Oxford Mathematical Monographs MR1402243 (97k:73001)* (The Clarendon Press, Oxford University Press, New York, 1993)
4. G. Bolling, W. Tiller, Growth from the Melt: Part 1. The Influence of Surface Intersections in Pure Metals. J. Appl. Phys. **31**, 1345 (1960)
5. J.R. Newman, *The World of Mathematics*, vol. 2 (Simon and Shuster, New York, 1956)
6. R. Courant, H. Robbins, *What is Mathematics?*, 2nd edn. (Oxford University Press, New York, Ch. IX, 1956)
7. M. Glicksman, Capillary Mediated Interface Perturbations: Deterministic Pattern Formation. J. Cryst. Growth **450**, 119–139 (2016)
8. M. Glicksman, K. Ankit, Detection of Capillary Mediated Energy Fields on a Grain Boundary Groove: Solid-Liquid Interface Perturbations. Metals **7**(12), 547–567 (2017)
9. M. Glicksman, K. Ankit, Measuring Solid-Liquid Interfacial Energy Fields: Diffusion Limited Patterns. J. Mat. Sci. **53**(17), 1–24 (2018)
10. M. Perez, Gibbs-Thomson Effects in Phase Transformation. Scripta Mater. **52**, 709–712 (2005)
11. R. Weinstock, *Calculus of Variations* (Dover Publications Inc, New York, 1974)
12. G. Nash, M. Glicksman, A General Method for Determining Solid-Liquid Interfacial Free Energies. Phil. Mag. **24**, 577 (1971)
13. M. Glicksman, *Principles of Solidification* (Springer, New York, 2011)
14. B. Bayender, N. Marasli, E. Cadirli, H. Sisman, M. Gündüz, Solid-Liquid Surface Energy of Pivalic Acid. J. Cryst. Growth **194**, 119–124 (1998)
15. B. Bayender, N. Marasli, E. Cadirli, M. Gündüz, Solid-Liquid Interfacial Energy of Camphene. Mat. Sci. and Engr. A **270**, 343–348 (1999)
16. R. DeHoff, *Thermodynamics in Materials Science, Materials Science and Engineering Series* (McGraw-Hill Inc., New York, 1953)
17. L. Kells, *Calculus*, 7th edn. (Prentice-Hall Inc, New York, 1946)
18. M. Glicksman, K. Ankit, Thermodynamic Behaviour of Solid-Liquid Grain Boundary Grooves. Philosophical Magazine **55**, 1–24 (2020)
19. I. Gradshteyn, I. Ryzhik, *Table of Integrals, Series, and Products* (Academic Press, New York, 1980)

J. Phase Equilib. Diffus. (2022) 43:718–737

737

20. A. Gray, E. Abbena, S. Salamon, *Modern Differential Geometry of Curves and Surfaces with Mathematica*, 3rd edn. (Chapman & Hall/CRC, Boca Raton, FL, 2006)

21. Y. Ocaka, S. Akbulut, U. Boyuk, M. Erol, K. Keslioglu, N. Marash, Solid-Liquid Interfacial Energy for Solid Succinonitrile in Equilibrium with Succinonitrile Dichlorobenzene Eutectic Liquid. Thermochimica Acta **445**, 86–91 (2006)

22. P. Buffat, J. Borel, Size Effect on the Melting Temperature of Gold Particles. Physical Review A **13**, 2287–2298 (1976)

23. P. Wu, K. Ankit, M. Glicksman, *Phase-Field Image Analysis of Periodic Grain Boundaries* (Unpublished research, Arizona State University, Tempe, AZ, 2021)

24. M. Glicksman, P. Wu, K. Ankit, Surface Laplacian of Interfacial Thermochemical Potential: Its Role in Solid-Liquid Pattern Formation. npj Microgravity **1**, 1–10 (2021)

25. J. Jackson, *Classical Electrodynamics*, 3rd edn. (John Wiley & Sons Inc, New York, NY, 1999)

26. D. Jones, The Measurement of Solid-Liquid Interfacial Energies from the Shapes of Grain-Boundary Grooves. Phil. Mag. **27**, 569 (1973)

27. R. Schaefer, M. Glicksman, J. Ayers, High-Confidence Measurement of Solid-Liquid Surface Energy in a Pure Material. Phil. Mag. **32**, 725–743 (1975)

28. S. Hardy, A Grain Boundary Groove Measurement of the Surface Tension Between Ice and Water. Phil. Mag. **35**, 471 (1977)

29. N. Noel, H. Jamgotchian, B. Billia, Influence of Grain Boundaries and Natural Convection on Microstructure Formation in Cellular Directional Solidification of Dilute Succinonitrile Alloys in a Cylinder. J. Cryst. Growth **187**, 516–526 (1998)

30. K. Keslioglu, N. Marasli, Experimental Determination of Solid-Liquid Interfacial Energy for Zinc Solid Solution in Equilibrium with the Zinc-Aluminum Eutectic Liquid. Met. and Mat. Trans. A **35**, 3665–3672 (2004)

31. R. Rogers, B. Ackerson, The Measurement of Solid-Liquid Interfacial Energy in Colloidal Suspensions Using Grain Boundary Grooves. Phil. Mag. **91**, 682–729 (2011)

32. M. Turing Alan, The Chemical Basis of Morphogenesis. Phil. Trans. R. Soc. Lond. B **237**, 37–72 (1952)